

# **Frustrated phonon with charge density wave in vanadium Kagome metal**

Seung-Phil Heo<sup>1,2,3</sup>, Choongjae Won<sup>4</sup>, Heemin Lee<sup>1,2,3</sup>, Hanbyul Kim<sup>5</sup>, Eunyoung Park<sup>1,2,3</sup>,  
Sung Yun Lee<sup>1,2,3</sup>, Junha Hwang<sup>1,2,3</sup>, Hyeonggi Choi<sup>6</sup>, Sang-Youn Park<sup>6</sup>, Byungjune Lee<sup>1,3,4</sup>,  
Woo-Suk Noh<sup>4,6</sup>, Hoyoung Jang<sup>3,6</sup>, Jae-Hoon Park<sup>1,3,4</sup>, Dongbin Shin<sup>5,7\*</sup>, Changyong Song<sup>1,2,3\*</sup>

<sup>1</sup>*Department of Physics, POSTECH, Pohang 37673, Korea.* <sup>2</sup>*Center for Ultrafast Science on Quantum Matter, Max Planck POSTECH/Korea Research Initiative, Pohang 37673, Korea.*

<sup>3</sup>*Photon Science Center, POSTECH 37673, Pohang 37673, Korea.* <sup>4</sup>*Center for Complex Phase Materials, Max Planck POSTECH/Korea Research Initiative, Pohang 37673, Korea.*

<sup>5</sup>*Department of Physics and Photon Science, Gwangju Institute of Science and Technology, Gwangju 61005, Korea.* <sup>6</sup>*Pohang Accelerator Laboratory, POSTECH, Pohang 37673, Korea.*

<sup>7</sup>*Max Planck Institute for the Structure and Dynamics of Matter, Hamburg 22761, Germany.*

**Crystals with unique ionic arrangements and strong electronic correlations serve as a fertile ground for the emergence of exotic phases, as evidenced by the coexistence of charge density wave (CDW) and superconductivity in vanadium Kagome metals, specifically  $AV_3Sb_5$  (where A represents K, Rb, or Cs). The formation of a star-of-David CDW superstructure, resulting from the coordinated displacements of vanadium ions on a corner-sharing triangular lattice, has garnered significant attention in efforts to comprehend the influence of electron–phonon interaction within this geometrically intricate lattice. However, understanding of the underlying mechanism behind CDW formation, coupled with symmetry-protected lattice vibrations, remains elusive. In this study, we employed time-resolved X-ray scattering experiments utilising an X-ray free electron laser. Our findings reveal that the phonon mode associated with the out-of-plane**

**motion of Cs ions becomes frustrated in the CDW phase. Furthermore, we observed the photoinduced emergence of a metastable CDW phase, facilitated by the alleviation of frustration through nonadiabatic changes in free energy. By elucidating the longstanding puzzle surrounding the intervention of phonons in CDW ordering, this research offers fresh insights into the competition between phonons and periodic lattice distortions, a phenomenon widespread in other correlated quantum materials including layered high- $T_C$  superconductors.**

Exotic phases involving CDW and superconductivity (SC), arising from intricate electronic structures within geometrically frustrated ionic arrangements, have spurred active investigation into the vanadium (V) Kagome metal  $AV_3Sb_5$  (where A represents K, Rb, and Cs) (Fig. 1a)<sup>1,2</sup>. Experimental findings suggest that mechanisms driving CDW formation extend beyond Peierls distortion, with enhanced electron–phonon interactions facilitated by nested Fermi surfaces. This has led to new hypotheses regarding electron–hole pairing mediated by phonons<sup>3–6</sup>. The van Hove singularity of V  $d$ -electrons near the Fermi level has been proposed as a pivotal factor in CDW instability<sup>7,8</sup>. However, the role of phonons remains ambiguous, as phonon softening, a characteristic of CDW instability, has not been observed<sup>5,9</sup>. Additionally, the CDW and SC phases exhibit sensitivity to different choices of alkali metal ions in the Kagome system<sup>10–14</sup>, despite the limited presence of electron population from the cations near the Fermi level<sup>7,8</sup>. These findings suggest that the electronic potential energy surface may undergo dramatic changes due to cation movement, giving rise to such diverse phases. However, research on the CDW phase in excited states has been lacking, leaving a gap in understanding the impact of cation dynamics on phase stability.

We conducted femtosecond (fs) time-resolved X-ray scattering experiments on  $CsV_3Sb_5$  to explore CDW instabilities existing within a finely balanced potential energy landscape, achieved by photoexciting conduction electrons using fs-infrared (IR) laser pulses.

X-ray scattering experiments were conducted utilising the Pohang Accelerator Laboratory X-ray Free Electron Laser (PAL-XFEL) and the Pohang Light Source (PLS). The emergence of superstructures below the CDW transition temperature of 96 K was confirmed, revealing the coexistent  $2\times 2\times 1$  and  $2\times 2\times 2$  CDWs (notated as  $a\times b\times c$  in multiples of the unit cell) (Figs. 1a and b)<sup>15</sup>. Doubling of the unit cell in the  $ab$ -plane resulted in a  $2\times 2$  superstructure due to in-plane displacements of V ions, forming a star-of-David (SoD) or its inverse triangle-and-hexagon (TrH) pattern (Fig. 1a)<sup>10,16,17</sup>. Additionally, unit cell doubling along the  $c$ -axis was observed, establishing the  $2\times 2\times 2$  superstructure. Another lattice instability is required to induce this superstructure with the phonon mode ( $L_2^-$ ) involving ions'  $c$ -directional motion attributed to driving this instability<sup>9,18</sup>. The  $2\times 2\times 1$  CDW was distinguishable from the  $2\times 2\times 2$  counterpart by different peak widths, as well as by the temperature dependence of the order parameters derived from the integrated intensities of the CDW satellites (Fig. 1b and Supplementary Note 1)<sup>5,6,19</sup>.

The rapid redistribution of electrons near the Fermi level due to fs-IR photoexcitation disturbed these CDW orderings. Subsequently, the ultrafast reaction dynamics of the CDWs were investigated using femtosecond X-ray pulses from the PAL-XFEL (Fig. 1c and Method). The temporal evolution of peak intensity from the  $2\times 2\times 2$  CDW reflection exhibited an oscillation without full recovery until approximately 2 ns, whereas no oscillation was observed for the  $2\times 2\times 1$  CDW (Fig. 1d). These features were explicitly resolved by simulating exponential decay and recovery reactions (drawn with a solid line) (Supplementary Note 2). Both CDWs underwent rapid melting at approximately 100 fs, followed by a quick yet partial recovery of intensity at around 300 fs. These time scales suggest electron–phonon interaction mediated CDWs<sup>20-22</sup>. After photoinduced melting, the CDWs remained in a metastable state for at least a couple of nanoseconds before fully recovering in less than 10 ms. Comparing this

with the stabilization of the thermalised lattice in several hundred picoseconds indicated that the metastable CDW phase persisted beyond thermal equilibration (Supplementary Note 3)<sup>23</sup>.

The oscillating intensity of the  $2\times 2\times 2$  CDW reflected a coherent phonon with a frequency of approximately 1.3 THz. This resembles aforementioned  $L_2^-$  phonon but with a critical difference<sup>9,18</sup>. Native  $L_2^-$  phonon involves symmetric motions of two Cs ions moving upward and the other two moving downward. However, such a symmetric vibration mode cannot induce any intensity change in the  $2\times 2\times 2$  superstructure reflection (Supplementary Note 4). Hence, the observed oscillatory intensity suggests a fundamental modification of the native  $L_2^-$  phonon caused by the fs-IR photoexcitation of conduction electrons. Consistent with this, the coherent phonons detected through CDW reflection exhibited an unusual phase delay of approximately  $\pi$  (Supplementary Note 2)<sup>24,25</sup>. This phase delay indicates the presence of competing interactions that delay the prompt excitation of coherent phonons and distort the native phonon mode<sup>26-28</sup>.

The emergence of strong diffuse signals along the  $c$ -direction around the  $2\times 2\times 2$  CDW reflection strongly supports the interpretation of competing interactions between the  $2\times 2\times 2$  CDW and the  $L_2^-$  phonon mode (Fig. 2a). The first diffuse streak, which developed at 200 fs, was of the ordinary type resulting from CDW melting, with a reduced domain size of approximately 60% of the intact value (Fig. 2b). As the peak sharpened with CDW reconstruction, another strong diffuse streak appeared at around 400 fs, coinciding with the delayed onset of the coherent phonon (Fig. 2b). This transiently formed diffuse signal, observed at approximately 400 fs, exhibited a two-wing structure relative to the main CDW reflection. These wings developed at positions with symmetric offsets ( $\pm \delta q \sim 5\times 10^{-3} 2\pi/c$ ) from the main  $2\times 2\times 2$  CDW at  $1.5 (2\pi/c)$  indicating a phase slip formed while relieving the frustrated phonon (Fig. 2b)<sup>29-31</sup>. Here, we present a schematic model describing the phase slip resulted from the asymmetric alterations: three-up (down) and one-down (up) deviated from the symmetric two-

up and two-down displacements (Fig. 2c). The proposed structural model was consistent with the diffuse scattering pattern developed along the  $c$ -direction, as shown in the inset (Supplementary Note 5).

This modification of the native  $L_2^-$  phonon mode after the photoexcitation was verified through time-dependent density functional theory (TD-DFT) calculations (Methods). TD-DFT revealed that the inversion of the displacement of one Cs ion was accompanied by fs-IR photoexcitation, resulting in a three-to-one vibration (Supplementary Note 6). This inversion of the Cs-ion displacement was also corroborated by potential energy surface calculations, indicating that the system reaches a lower energy state with the Cs ions at the centre of TrH (or SoD) moving toward (out of) the V superstructure (Fig. 2e). The calculation confirmed an energy gain of 6 meV by displacing the Cs ions toward the TrH centre by 0.1 Å compared to the original position (Fig. 2e). In the native  $L_2^-$  phonon mode, for the paired Cs ions, one ion was situated at the centre of the SoD (or TrH), whereas the other was not (Fig. 2d). Therefore, the native  $L_2^-$  phonon mode with two-up and two-down vibrations was incompatible with the lower energy configuration, thus being frustrated in the CDW phase. With a significant perturbation of the potential energy by restructuring the CDW using the fs-IR laser, the frustration was alleviated by inverting the movement of one Cs ion to align with the lower total energy configuration of the CDW phase. This resulted in asymmetric three-up (down) and one-down (up) vibrations, consistent with the observation of the oscillatory intensity of the  $2\times 2\times 2$  CDW reflection (Fig. 2d).

To comprehend the impact of photoexcited electrons on frustrated phonons and CDW instability systematically, we explored the fluence dependence of fs-IR pump laser (Fig. 3). A more pronounced reduction in peak intensities was consistently observed owing to increased CDW melting with higher laser fluence (Fig. 3a). The response times for melting and subsequent short recovery appeared relatively unaffected by variations in laser fluence ranging

from 0.05 to 2.5 mJ cm<sup>-2</sup> (Figs. 3c and d). The melting time remained approximately 100 fs, displaying minimal dependence on laser fluence (Fig. 3c). This time scale aligns with nesting-mediated CDWs, supporting the notion that both CDWs are primarily formed by electron–phonon interaction<sup>20-22</sup>. Following this melting, there was a prompt intensity recovery, yet it failed to fully return to the intact state with the reopening of the CDW gap. This rapid recovery occurred at ~ 300 fs, consistent with both the 2×2×1 and 2×2×2 CDWs (Fig. 3d).

The fluence-dependent intensity of the 2×2×2 CDW exhibited intriguing characteristics warranting further investigation. Following the initial reduction upon melting, the intensity rebounded to its maximum value, showing a discernible dependence on laser fluence (Figs. 3a and b). For laser fluences exceeding approximately 0.5 mJ cm<sup>-2</sup>, the intensity surpassed the intact state, denoted as 'overdamped CDW'. This transient CDW overdamping was similarly observed in other layered transition metal compounds exhibiting SoD CDW<sup>32,33</sup>. Subsequent to overdamping at around 400 fs, the intensity oscillated around a mean value lower than the intact state, without full recovery, persisting in a metastable state for several nanoseconds<sup>18,34,35</sup>. The intensity reduction in this metastable state increased with IR laser fluence until reaching approximately 1.4 mJ cm<sup>-2</sup>, with a fluence dependence akin to that of the overdamped CDW intensity (Fig. 3b). Overall, the oscillation frequency of the modified coherent phonon remained largely unaffected by laser fluence, exhibiting only weak softening (1.5%) (Supplementary Note 7)<sup>5,9,22</sup>.

We present a visual representation summarizing the overall photoinduced melting and metastable configuration of the 2×2×2 CDW (Fig. 4). The harmonic potential of the ions is schematically depicted for the CDW amplitude or mean ionic displacement ( $A$ ). The potential energy of the intact 2×2×2 CDW exhibited a ground state with an initial CDW amplitude of  $A_0$  (Fig. 4a)<sup>34</sup>. Fs-IR laser pumping shifted the potential energy surface (PES) to the ground state without a CDW ( $A = 0$ ), indicating photoinduced gap closing ( $t \sim 0$ ). With this transiently

formed PES, the CDW melted to reach the ground state ( $\omega t \sim \pi/2$ )<sup>35</sup>. While adapting to this new PES, CDW overdamping occurred at  $\omega t \sim \pi$  with displacement  $A_{OD}$ , further shifting the PES to a metastable ground state at  $A_{MS}$ . The new CDW then oscillated around the metastable ground state with an amplitude  $A_{MS}$  smaller than  $A_0$ , as observed experimentally<sup>18,36,37</sup>. Corresponding atomic configurations are depicted (Fig. 4b). The intact CDW, characterised by two-up and two-down displacements of Cs ions relative to the V-dimerised CDW, demonstrated frustration. Upon femtosecond modification of the electron distribution by fs-IR photoexcitation, the symmetric (two-up and two-down) phonon mode, previously frustrated, was relieved, inducing up (down) and one-down (up) vibrations compatible with the potential energy surface.

In summary, we investigated the ultrafast dynamics of CDWs in the excited PES of  $\text{CsV}_3\text{Sb}_5$  by transiently redistributing electrons near the Fermi levels using an fs-IR laser pulse. Through fs-IR photoexcitation, we induced a metastable CDW phase with a localised phonon mode, relieving the energetically frustrated two-up and two-down vibrations of Cs ions in the CDW state. This phonon mode, characterised by symmetric out-of-plane displacements of alkali ions, leads to energy loss directly coupled with the dimerization of V ions within the Kagome net, resulting in phonon frustration in the CDW phase. Restructuring the CDW using fs-IR laser photoexcitation relieves this phonon frustration, inducing a frustration-relieved localised phonon mode in a metastable CDW state. Our study unveiled the intricate coupling of phonons in this strongly correlated flat-band system with exotic CDW phases by directly observing the modified asymmetric coherent phonons formed in a transiently disturbed potential energy landscape. It provides a concrete understanding of the mysterious roles of phonons in Kagome metals, emphasizing the crucial role of alkali ions in controlling CDW ordering<sup>10-14</sup>. Additionally, we note that this discovery shares common ground with

understanding the energetics behind exotic charge ordering in layered high- $T_C$  superconductors and other two-dimensional dichalcogenide materials<sup>38–42</sup>.

## References

1. Zhao, H. *et al.* Cascade of correlated electron states in the kagome superconductor  $\text{CsV}_3\text{Sb}_5$ . *Nature* **599**, 216–221 (2021).
2. Nie, L. *et al.* Charge-density-wave-driven electronic nematicity in a kagome superconductor. *Nature* **604**, 59–64 (2022).
3. Jiang, Y.-X. *et al.* Unconventional chiral charge order in kagome superconductor  $\text{KV}_3\text{Sb}_5$ . *Nat. Mater.* **20**, 1353–1357 (2021).
4. Kang, M. *et al.* Twofold van Hove singularity and origin of charge order in topological kagome superconductor  $\text{CsV}_3\text{Sb}_5$ . *Nat. Phys.* **18**, 301–308 (2022).
5. Li, H. *et al.* Observation of Unconventional Charge Density Wave without Acoustic Phonon Anomaly in Kagome Superconductors  $\text{AV}_3\text{Sb}_5$  ( $A = \text{Rb}, \text{Cs}$ ). *Phys. Rev. X* **11**, 031050 (2021).
6. Grüner, G. *Density waves in solids* (Westview Press, 2009).
7. Tan, H., Liu, Y., Wang, Z. & Yan, B. Charge Density Waves and Electronic Properties of Superconducting Kagome Metals. *Phys. Rev. Lett.* **127**, 046401 (2021).
8. Ortiz, B. R. *et al.* Fermi Surface Mapping and the Nature of Charge-Density-Wave Order in the Kagome Superconductor  $\text{CsV}_3\text{Sb}_5$ . *Phys. Rev. X* **11**, 041030 (2021).
9. Subires, D. *et al.* Order-disorder charge density wave instability in the kagome metal  $(\text{Cs,Rb})\text{V}_3\text{Sb}_5$ . *Nat. Commun.* **14**, 1015 (2023).
10. Kang, M. *et al.* Charge order landscape and competition with superconductivity in kagome metals. *Nat. Mater.* **22**, 186–193 (2023).
11. Ortiz, B. R. *et al.* New kagome prototype materials: discovery of  $\text{KV}_3\text{Sb}_5$ ,  $\text{RbV}_3\text{Sb}_5$ , and  $\text{CsV}_3\text{Sb}_5$ . *Phys. Rev. Mater.* **3**, 094407 (2019).
12. Ortiz, B. R. *et al.*  $\text{CsV}_3\text{Sb}_5$  A  $\mathbb{Z}_2$  Topological Kagome Metal with a Superconducting Ground State. *Phys. Rev. Lett.* **125**, 247002 (2020).



13. Ortiz, B. R. *et al.* Superconductivity in the  $Z_2$  kagome metal  $KV_3Sb_5$ . *Phys. Rev. Mater.* **5**, 034801 (2021).
14. Yin, Q. *et al.* Superconductivity and Normal-State Properties of Kagome Metal  $RbV_3Sb_5$  Single Crystals. *Chin. Phys. Lett.* **38**, 037403 (2021).
15. Li, H. *et al.* Discovery of conjoined charge density waves in the kagome superconductor  $CsV_3Sb_5$ . *Nat. Commun.* **13**, 6348 (2022).
16. Christensen, M. H., Birol, T., Andersen, B. M. & Fernandes, R. M. Theory of the charge density wave in  $AV_3Sb_5$  kagome metals. *Phys. Rev. B* **104**, 214513 (2021).
17. Hu, Y. *et al.* Coexistence of trihexagonal and star-of-David pattern in the charge density wave of the kagome superconductor  $AV_3Sb_5$ . *Phys. Rev. B* **106**, L241106 (2022).
18. Ratcliff, N., Hallett, L., Ortiz, B. R., Wilson, S. D. & Harter, J. W. Coherent phonon spectroscopy and interlayer modulation of charge density wave order in the kagome metal  $CsV_3Sb_5$ . *Phys. Rev. Mater.* **5**, L111801 (2021).
19. Song, C. *et al.* Charge-density-wave orderings in  $LaAgSb_2$ : An x-ray scattering study. *Phys. Rev. B* **68**, 035113 (2003).
20. Rohwer, T. *et al.* Collapse of long-range charge order tracked by time-resolved photoemission at high momenta. *Nature* **471**, 490–493 (2011).
21. Hellmann, S. *et al.* Time-domain classification of charge-density-wave insulators. *Nat Commun.* **3**, 1069 (2012).
22. Azoury, D. *et al.* Direct Observation of Collective Modes of the Charge Density Wave in the Kagome Metal  $CsV_3Sb_5$ . PNAS <https://doi.org/10.1073/pnas.2308588120> (2023).
23. Allen, P. B. Theory of thermal relaxation of electrons in metals. *Phys. Rev. Lett.* **59**, 1460–1463 (1987).
24. Zeiger, H. J., *et al.* Theory for dispersive excitation of coherent phonons. *Phys. Rev. B* **45**, 768–778 (1992).
25. Garrett, G. A., Albrecht, T. F., Whitaker, J. F. & Merlin, R. Coherent THz Phonons Driven by Light Pulses and the Sb Problem: What is the Mechanism? *Phys. Rev. Lett.* **77**, 3661–3664 (1996).

26. Sokolowski-Tinten, K., *et al.* Femtosecond X-ray measurement of coherent lattice vibrations near the Lindemann stability limit. *Nature* **422**, 287–289 (2003).
27. Fritz, D. M. *et al.* Ultrafast Bond Softening in Bismuth: Mapping a Solid’s Interatomic Potential with X-rays. *Science* **315**, 633–636 (2007).
28. Huber, T. *et al.* Coherent Structural Dynamics of a Prototypical Charge-Density-Wave-to-Metal Transition. *Phys. Rev. Lett.* **113**, 026401 (2014).
29. Cheng, Y. *et al.* Ultrafast formation of topological defects in a two-dimensional charge density wave. *Nat. Phys.* **20**, 54–60 (2024).
30. Vinograd, I. *et al.* Locally commensurate charge-density wave with three-unit-cell periodicity in  $\text{YBa}_2\text{Cu}_3\text{O}_y$ . *Nat. Commun.* **12**, 3274 (2021).
31. Kim, H. J., *et al.* Local Atomic Structure and Discommensurations in the Charge Density Wave of  $\text{CeTe}_3$ . *Phys. Rev. Lett.* **96**, 226401 (2006).
32. Zhang, Y., *et al.* Creation of a novel inverted charge density wave state. *Struct. Dyn.* **9**, 014501 (2022).
33. Zhang, J., *et al.* Photoexcitation Induced Quantum Dynamics of Charge Density Wave and Emergence of a Collective Mode in  $1T\text{-TaS}_2$ . *Nano Lett.* **19**, 6027–6034 (2019).
34. Littlewood, P. B. & Varma, C. M. Amplitude collective modes in superconductors and their coupling to charge-density waves. *Phys. Rev. B* **26**, 4883–4893 (1982).
35. Singer, A., *et al.* Photoinduced Enhancement of the Charge Density Wave Amplitude. *Phys. Rev. Lett.* **117**, 056401 (2016).
36. Yu, J., *et al.* All-optical manipulation of charge density waves in kagome metal  $\text{CsV}_3\text{Sb}_5$ . *Phys. Rev. B* **107**, 174303 (2023).
37. Mihaly, L., Lee, K.-B. & Stephens, P. W. X-ray diffraction study of the metastable charge-density-wave state of  $\text{K}_{0.3}\text{MoO}_3$ . *Phys. Rev. B* **36**, 1793–1795 (1987).
38. Cao, Y., *et al.* Unconventional superconductivity in magic-angle graphene superlattices. *Nature* **556**, 43–50 (2018).
39. Si, Q., Yu, R. & Abrahams, E. High-temperature superconductivity in iron pnictides and chalcogenides *Nat. Rev. Mater.* **1**, 16017 (2016).

40. Kogar, A., *et al.* Light-induced charge density wave in  $\text{LaTe}_3$ . *Nat. Phys.* **16**, 159–163 (2020).
41. Disa, A. S., Nova, T. F. & Cavalleri, A. Engineering crystal structures with light. *Nat. Phys.* **17**, 1087–1092 (2021).
42. Fausti, D., *et al.* Light-Induced Superconductivity in a Stripe-Ordered Cuprate. *Science* **331**, 189–191 (2011).

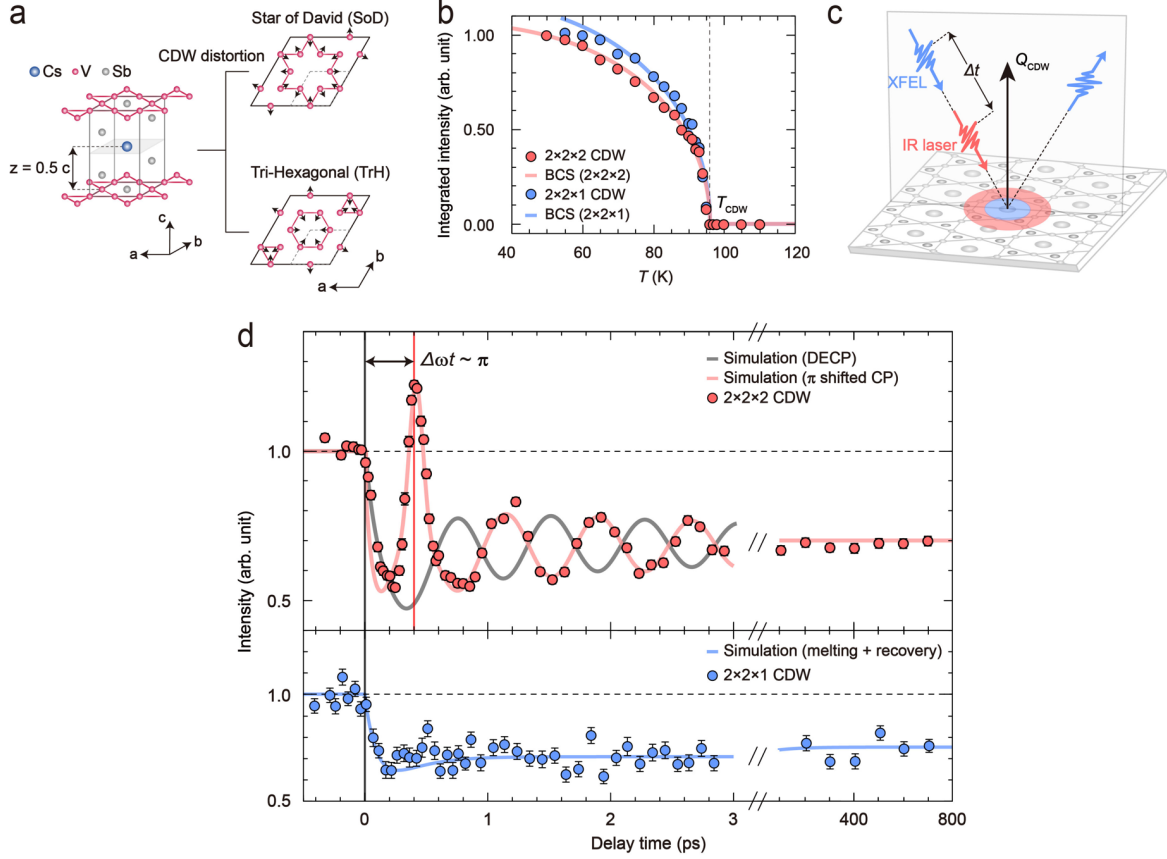


**Fig. 1: Time-resolved X-ray scattering investigation of CDW superstructures of  $\text{CsV}_3\text{Sb}_5$ .**

**a.** Crystal structure of  $\text{CsV}_3\text{Sb}_5$  with the vanadium-networked Kagome lattice. **b.** CDW order parameters derived from the integrated intensities of the  $(0.5\ 0\ 2)$  and  $(0.5\ 0\ 1.5)$  reflections representing the  $2\times 2\times 1$  and  $2\times 2\times 2$  superstructures, respectively. Solid lines depict results from BCS gap equations. **c.** Schematic representation of time-resolved X-ray scattering experiments. **d.** Temporal evolution of the  $2\times 2\times 1$  and  $2\times 2\times 2$  CDW reflections showing photoinduced melting and recovery. Ultrafast melting within 100 fs is commonly observed for both  $2\times 2\times 1$  and  $2\times 2\times 2$ , with the peak intensity not fully recovering immediately. Solids lines are from simulations (text). Notably, intensity oscillation is observed for the  $2\times 2\times 2$  CDW. It results from a coherent phonon oscillation (red line) but with a phase delay of  $\omega t \sim 400$  fs, distinguished from normal displacement excited coherent phonon (DECP, grey line)

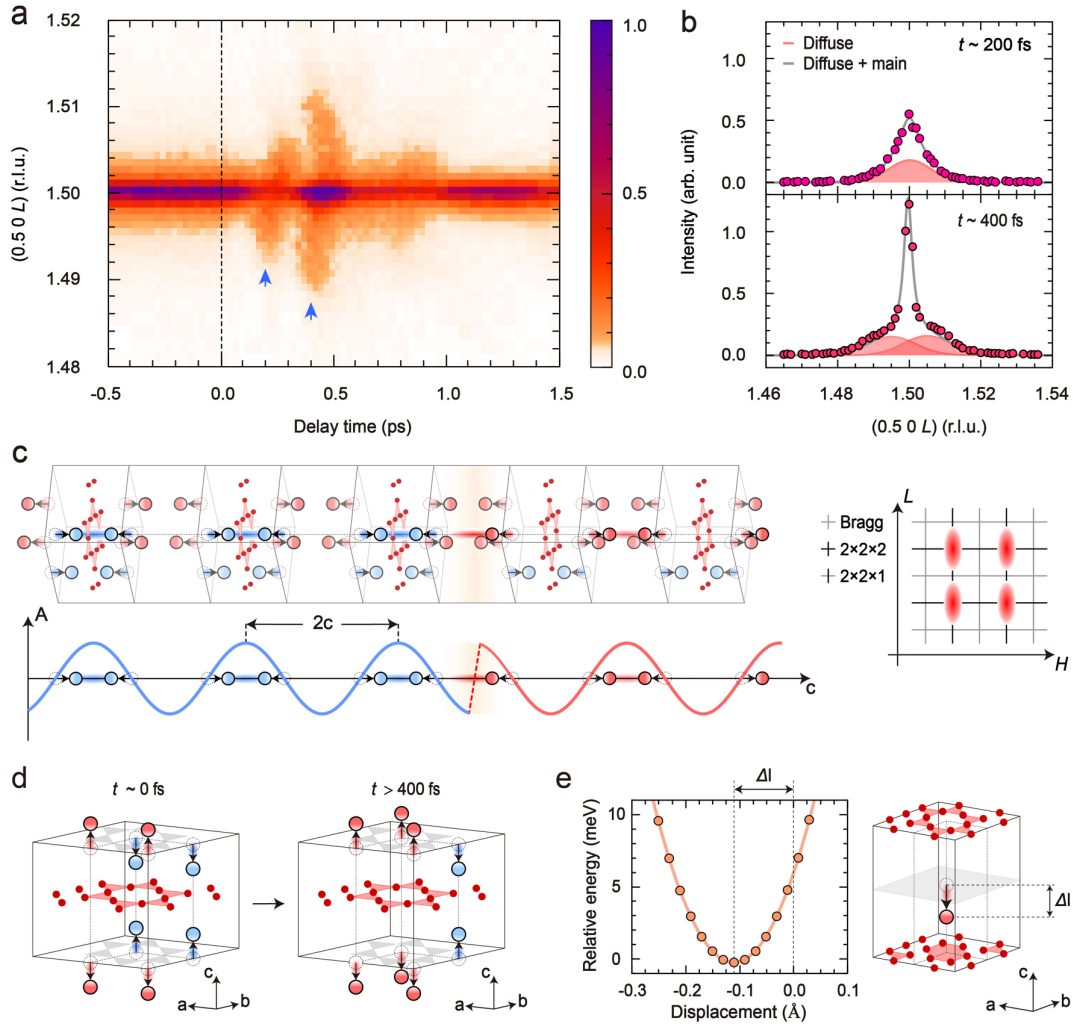


**Fig. 2: Metastable CDW states with localised phonon mode. a.** Photoinduced melting of the  $2 \times 2 \times 2$  CDW with strong diffuse signals developed along the  $c$ -direction at  $\sim 200$  fs and 400 fs (blue arrows). **b.** The  $L$ -scan at 400 fs displays diffusive two-wing structure, centered on  $2 \times 2 \times 2$  CDW reflection, caused by a phase slip in the CDW domain (lower panel), distinguishable from the signal at 200 fs with diffuse tails resulting from reduced domain size (upper panel). **c.** Phase-slip in the  $2 \times 2 \times 2$  CDW. The red-coloured sinusoidal wave indicates the domain with three-one Cs displacements newly formed from the native two-two vibration (blue colour). Right panel displays the diffuse scattering pattern corresponding to this phase-slip structure. **d.** Comparison between the symmetric but energetically frustrated two-two vibration in the native CDW and the modified, frustration-relieved Cs vibration initiated at  $\sim 400$  fs, which persists

as a metastable CDW ordering. e. Potential energy surface calculation with an eye-guide solid line demonstrates that Cs ions, located at the centre of the  $2\times 2$  dimerised V structure, become more stable by moving toward (or out of) the TrH (SoD) mesh.

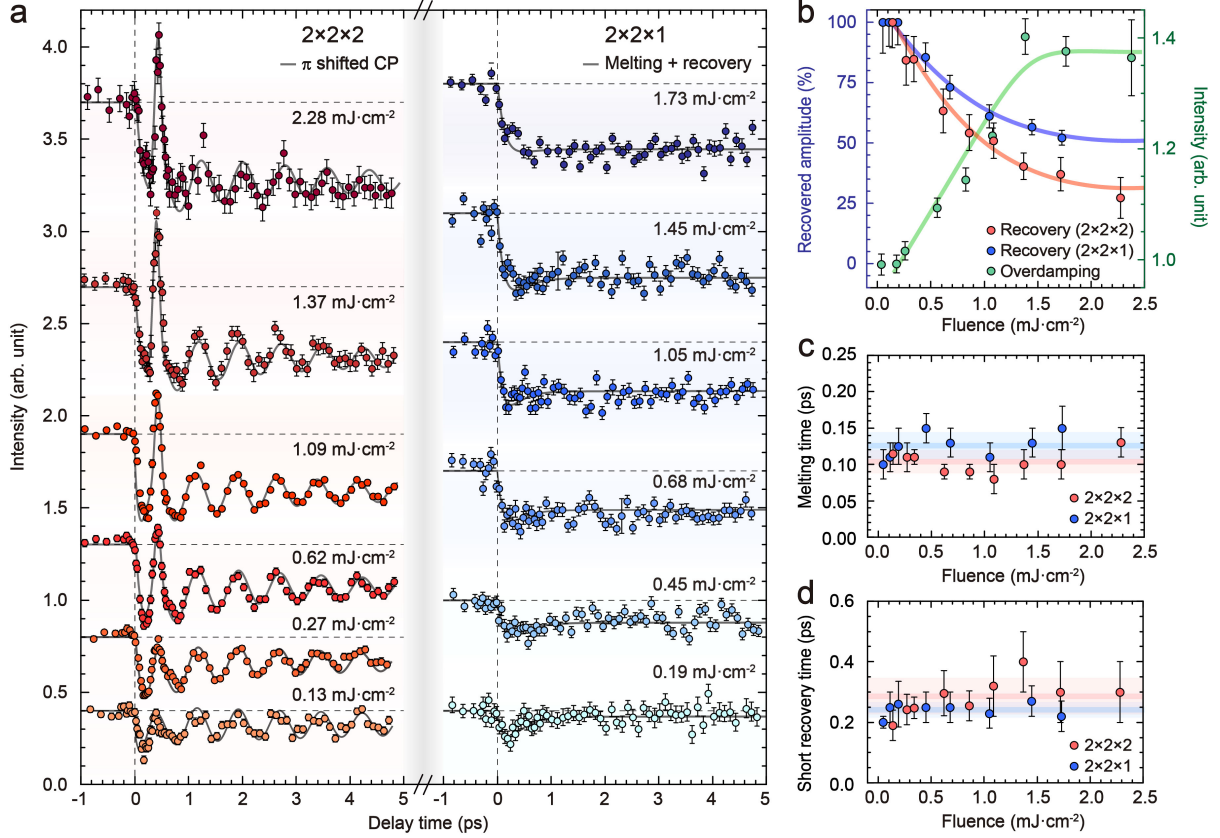


**Fig. 3: Laser fluence dependence of CDW melting and recovery.** **a.** Laser fluence dependence of the  $2 \times 2 \times 2$  (left) and  $2 \times 2 \times 1$  CDW (right) peak intensities, showing a larger reduction in peak intensities with higher laser fluence. Overdamped intensity at  $\sim 400$  fs develops more strongly in the  $2 \times 2 \times 2$  CDW with increasing laser fluence, but the oscillation period is insensitive to the laser fluence. **b.** Intensities of partially recovered CDWs obtained for different laser fluences, showing a similar behaviour of gradual decrease until  $\sim 1.4 \text{ mJ} \cdot \text{cm}^{-2}$  before saturation. Intensity of the overdamped oscillation at 400 fs is also compared, displaying a similar pattern of monotonic increase until  $1.4 \text{ mJ} \cdot \text{cm}^{-2}$  followed by saturation (right). **c-d.** Comparison of melting and short recovery time of the two CDWs, displaying a similar timescale for melting in 100 fs and short recovery in  $\sim 300$  fs without notable dependence on laser fluence. Solid lines, in b to d, are guide to eyes.

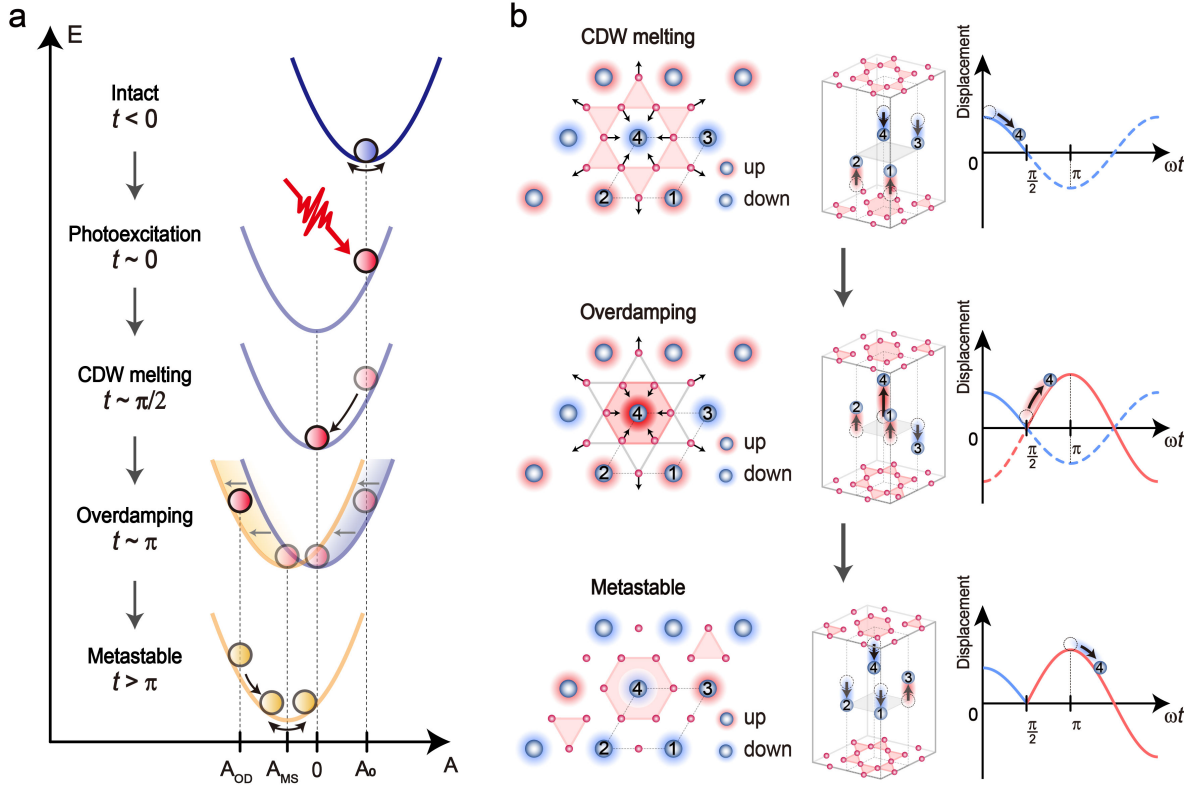


**Fig. 4: Photoinduced overdamping and metastable state of  $2 \times 2 \times 2$  CDW.** **a.** Ultrafast reaction in the  $2 \times 2 \times 2$  CDW depicted by a pictorial view of photoinduced potential energy changes with the CDW amplitude ( $A$ ). Fs-IR pumping shifts the potential energy to the ground state without CDW ( $A = 0$ ) caused by photoinduced gap closing ( $t \sim 0$ ). Following this transiently formed potential energy, the CDW melts to reach the energy ground state ( $\omega t \sim \pi/2$ ). While adapting to this new potential, overdamped displacement of the CDW occurs ( $\omega t \sim \pi$ ) with further displacement of the potential energy surface having the ground state at  $A_{MS}$ . The CDW amplitude now oscillates around the new ground state amplitude,  $A_{MS}$ , of the metastable state. **b.** Fs-IR pumping alters Cs ions'  $c$ -directional vibration ( $L_2^-$  phonon) in a manner to relieve energetically frustrated two-two displacements. Upon abrupt disturbance of the electron distribution by fs-IR pumping, the frustrated symmetric (two-up and two-down) phonon mode changes to three-one, compatible with the total energy.



## Methods

### Single crystal growth

Single-crystals of  $\text{CsV}_3\text{Sb}_5$  were grown using typical self-flux methods<sup>11,12</sup>. Owing to the highly reactive nature of elemental Cs, the subsequent preparation of  $\text{CsV}_3\text{Sb}_5$  was conducted inside an argon-filled glove box. Cs liquid (99.98% Alfa Aesar), acid-etched vanadium granules (99.7% Alfa Aesar), and Sb shots (99.99% Alfa Aesar) were placed in alumina crucibles with frit discs, then sealed in Ar-gas purged evacuated quartz tubes. The ampule was heated to 1000 °C for 24 h, then slowly cooled to 600 °C at a cooling rate of 5–3 °C/h. The ampule was then centrifuged to remove the flux, with any remaining flux removed via mechanical cleavage.

### Time-resolved X-ray scattering experiments

Time-resolved X-ray scattering (tr-XRS) experiments were conducted at the resonant soft X-ray scattering end station of the PAL-XFEL<sup>43</sup>. A single-crystal specimen of  $\text{CsV}_3\text{Sb}_5$ , with its surface normal parallel to the  $c$ -axis, was mounted on the cold finger of a liquid helium cryostat (base temperature  $\sim 20$  K). The diffractometer was aligned to have a horizon scattering plane with the sample  $ac$  plane and  $\pi$ -polarised incoming X-rays. X-ray pulses had a full width at half maximum pulse duration of approximately 80 fs and a repetition rate of 60 Hz. Incident X-ray photon energies were chosen to target the CDW superstructure reflections: 1240 eV for the  $2\times 2\times 2$  CDW at  $(0.5\ 0\ 1.5)$  reflection and 980 eV for the  $2\times 2\times 1$  CDW at  $(0.5\ 0\ 1)$ . IR photoexcitation of the specimen was induced using a femtosecond Ti:sapphire laser system (wavelength of 800 nm and pulse duration of 50 fs root-mean-square value). The mechanical delay stage controlled the time delay between the pump and probe pulses. The focused X-ray spot size at the sample position was  $100\ (\text{H}) \times 200\ (\text{V})\ \mu\text{m}^2$ , safely within the fs-IR laser

footprint of  $500 \text{ (H)} \times 500 \text{ (V)} \mu\text{m}^2$ . Each single-shot X-ray scattering signal was collected using an avalanche photodiode equipped with a high-speed digitiser. For all data collection processes, data were acquired at 30 Hz by interleaving pulses for data without laser pulses to ensure the full recovery of the specimen.

### **X-ray scattering measurement with temperature dependence**

The CDW order parameters were determined from the integrated intensity of the CDW reflections through X-ray scattering experiments conducted at the synchrotron 6A beamline of the PLS. Crystals were cryo-cooled using a liquid helium cryostat. The photon energy was fixed at 1580 eV, covering the  $2 \times 2 \times 2$  (0.5 0 1.5) and  $2 \times 2 \times 1$  (0.5 0 2) reflections.

### **Time-dependent density functional calculation**

To investigate the total energy, optimised lattice parameters, and electronic structure in the ground state of  $\text{CsV}_3\text{Sb}_5$  through first-principles calculations, density functional theory calculations were performed using the Quantum Espresso package<sup>44</sup>. The optimised lattice parameters for the  $2 \times 2 \times 2$  trigonal  $\text{CsV}_3\text{Sb}_5$  system were  $a = 10.88 \text{ \AA}$  and  $c = 18.66 \text{ \AA}$ . Kohn-Sham wave functions were illuminated by a plane wave with an energy cut-off of 60 Ry. The Perdew (Burke) Ernzerhof generalised gradient approximation functional was employed to describe electron-electron exchange and correlations<sup>45</sup>. Core electrons and their effects on valence electrons were addressed using norm-conserving pseudopotentials. The Brillouin zone was sampled using a Monkhorst pack with a  $3 \times 3 \times 2$  mesh. Ionic structure relaxation was achieved by optimising positions with the force criteria of  $1.0 \times 10^{-5} \text{ eV \AA}^{-1}$ .

To investigate light-induced dynamics using a first-principles approach, we employed Ehrenfest dynamics with real-time TD-DFT<sup>46</sup>. For time propagation, we utilised a Crank-Nicolson-type time-evolution operator with a time step of 4.8 attoseconds. The optimised Alternative SoD and TrH superstructures<sup>10,16</sup> served as the initial geometries for the TD-DFT calculations. An oscillating electric field of gaussian-packet type ( $E(t)$ ) was applied to the system through the vector potential term, with  $E(t) = dA/dt$  with  $A(t) = A_0 e^{-0.5 [(t-t_0)/\sigma]^2} \sin \omega t$ . The laser parameters in the simulation were set to match experimental conditions:  $\hbar\omega = 1.54$  eV and  $\sigma = 80$  fs, with a laser power density of  $3.6 \times 10^{10}$  W cm<sup>-2</sup>. The detailed calculation settings mirrored those of the DFT calculations, except for the Brillouin zone sampling ( $1 \times 1 \times 1$ ).

### Data Availability

The data supporting the findings of this study are available from the corresponding authors upon the request.

### Methods only references

43. Jang, H., *et al.* Time-resolved resonant elastic soft x-ray scattering at Pohang Accelerator Laboratory X-ray Free Electron Laser. *Rev. Sci. Instrum.* **91**, 083904 (2020).
44. Giannozzi, P., *et al.* QUANTUM ESPRESSO: A modular and open-source software project for quantum simulations of materials. *J. Phys. Condens. Matter* **21**, 395502 (2009).
45. Perdew, J. P., Burke, K. & Ernzerhof, M. Generalized Gradient Approximation Made Simple. *Phys. Rev. Lett.* **77**, 3865–3868 (1996).

46. Shin, D., Lee, G., Miyamoto, Y. & Park, N. Real-Time Propagation via Time-Dependent Density Functional Theory Plus the Hubbard U Potential for Electron–Atom Coupled Dynamics Involving Charge Transfer. *J. Chem. Theory Comput.* **12**, 201–208 (2016).

## **Acknowledgements**

C.S. appreciates Prof. K.-W. Kim for insightful discussion on the coherent phonon dynamics and Prof. G.-D. Lee on the abnormal lattice vibrations of interlayer alkali metal ions. X-ray scattering experiments at PAL are approved by the Korean Synchrotron Users Association (KOSUA). This work was supported by the National Research Foundations (NRF) of Korea (grant Nos. 2020K1A3A7A09080405, 2022M3H4A1A04074153, RS-2024-00346711, RS-2024-00333664 and RS-2023-00241630). The computational work was supported by the National Supercomputing Center with supercomputing resources including technical support (KSC-2023-CRE-0073).

## **Contributions**

C.S. supervised the project. C.S. and J.-H.P. conceived the project. S.-P.H., H.L., E.P., S.Y.L., J.H., B.L. H.J., and W.-S.N. performed the X-ray scattering experiments. C.W. synthesized the crystals. S.-P.H., H.L., and C.S. analyzed the data. H.C. maintained the fs-IR laser. S.Y.P. worked on the DAQ system. H.K. and D.S. performed the first-principle calculations. S.-P.H. and C.S. wrote the manuscript with input from all authors.

## **Corresponding authors**

Correspondence should be addressed to D.S. and C.S.

## **Competing interests**

The authors declare no competing interests.

## **Supplementary information**

# **Frustrated phonon with charge density wave in vanadium**

## **Kagome metal**

### **Authors:**

Seung-Phil Heo, Choongjae Won, Heemin Lee, Hanbyul Kim, Eunyoung Park, Sung Yun Lee, Junha Hwang, Hyeonggi Choi, Sang-Youn Park, Byungjune Lee, Woo-Suk Noh, Hoyoung Jang, Jae-Hoon Park, Dongbin Shin\*, Changyong Song\*

## Supplementary Note 1. Longitudinal scans along the $c$ -axis in coexisting CDW orderings.

Longitudinal scans along the  $(0\ 0\ L)$  direction are obtained around the  $(0.5\ 0\ 1.5)$  and  $(0.5\ 0\ 2)$  superstructure reflections, representing the  $2\times 2\times 2$  and  $2\times 2\times 1$  CDW, respectively (Fig. S1).

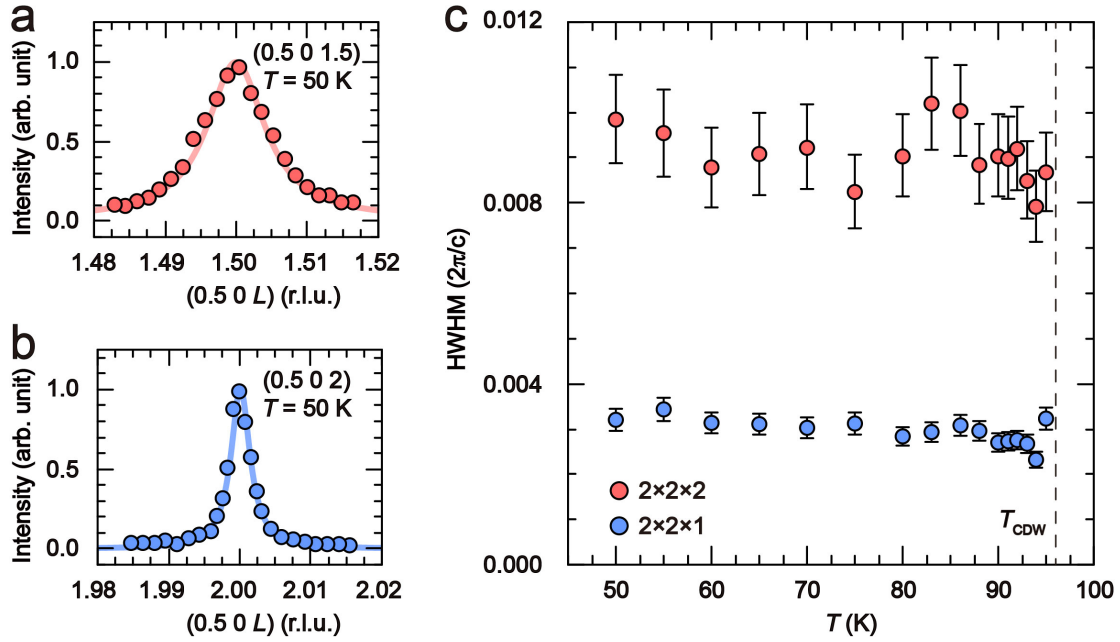


**Figure S1.**  $L$ -directional scans of  $2\times 2\times 2$  and  $2\times 2\times 1$  CDW. **a-b**,  $c$ -directional scan around the CDW superstructures of  $Q_{CDW}^{2\times 2\times 2}$  at  $(0.5\ 0\ 1.5)$  and  $Q_{CDW}^{2\times 2\times 1}$  at  $(0.5\ 0\ 2)$ , data taken at 50 K. **c**, Temperature dependence of the X-ray scattering peak width for the two CDW reflections showing the domain size along the  $c$ -direction is obtained. Larger peak width is noted for the  $2\times 2\times 2$  CDW implying smaller domain size along the  $c$ -direction, and no qualitative change in the domain size is noted throughout the temperature range in the CDW phase.

## Supplementary Note 2. Temporal evolution of the photo-melted CDW reflections

Temporal evolutions of the superstructure reflections for the  $2\times 2\times 1$  and  $2\times 2\times 2$  CDWs are quantified by simulating the time dependent intensity variation with the following relations:

$$I_{norm}(t) = 1 - A_{melt} \left( 1 - \exp \left[ -\frac{(t-t_0)}{\tau_{melt}} \right] \right) \\ + A_{short} \left( 1 - \exp \left[ -\frac{(t-t_0)}{\tau_{short}} \right] \right) + A_{long} \left( 1 - \exp \left[ -\frac{(t-t_0)}{\tau_{long}} \right] \right).$$

Here,  $I_{norm}(t)$ , represents the intensity normalized to the intact intensity value,  $A_{melt}(\tau_{melt})$ ,  $A_{short}(\tau_{short})$  and  $A_{long}(\tau_{long})$  are amplitude (time) of the melting, short recovery and long-time recovery in order. Whilst the  $2 \times 2 \times 1$  CDW is well described by this simple relaxation function, dynamics of the  $2 \times 2 \times 2$  CDW involves further complexity due to the coherent phonon oscillation requiring additional terms in simulating the intensity.

The coherent phonon oscillation and overdamped peak are considered with the following relation:

$$I_{norm}(t) = 1 - A_{melt} \left( 1 - \exp \left[ -\frac{(t-t_0)}{\tau_{melt}} \right] \right) \\ + A_{short} \left( 1 - \exp \left[ -\frac{(t-t_0)}{\tau_{short}} \right] \right) + A_{long} \left( 1 - \exp \left[ -\frac{(t-t_0)}{\tau_{long}} \right] \right) \\ + H(t-t_0) * A_{osc} \exp \left[ -\frac{(t-t_0)}{\tau_{osc}} \right] * \cos[2\pi f(t-t_0) + \pi] \\ + A_{OD} \exp \left[ -\frac{1}{2} \frac{(t-\tau_{OD})^2}{\sigma^2} \right].$$

Here,  $A_{osc}(\tau_{osc})$  and  $A_{OD}(\tau_{OD})$  are amplitude (characteristic time) of the coherent phonon oscillation and overdamped CDW recovery, respectively. Phonon frequency is noted by  $f$ . It should be noted that a phase delay of  $\pi$  in coherent phonon oscillation is essential to interpret intensity to launch the delayed phonon at  $\sim 400$  fs ( $2\pi \times 1.3$  THz  $\times 400$  fs  $\sim \pi$ ) (Fig. 1d).

### Supplementary Note 3. Temporal evolution of the Bragg reflection.

The temporal evolution of the (0 0 1) Bragg reflection intensity is displayed in Fig. S2, where we used the following function to simulate:

$$I_{norm}(t) = 1 - A_{melt} \left( 1 - \exp \left[ -\frac{(t-t_0)}{\tau_{melt}} \right] \right) + A_{rec} \left( 1 - \exp \left[ -\frac{(t-t_0)}{\tau_{rec}} \right] \right).$$

In the case of Bragg reflection, the melting time of  $\tau_{melt}$  ranges between 50 and 60 ps consistent with ordinary lattice melting time scale<sup>1</sup>. The incident laser fluence is approximately 1.6 mJ cm<sup>-2</sup>.

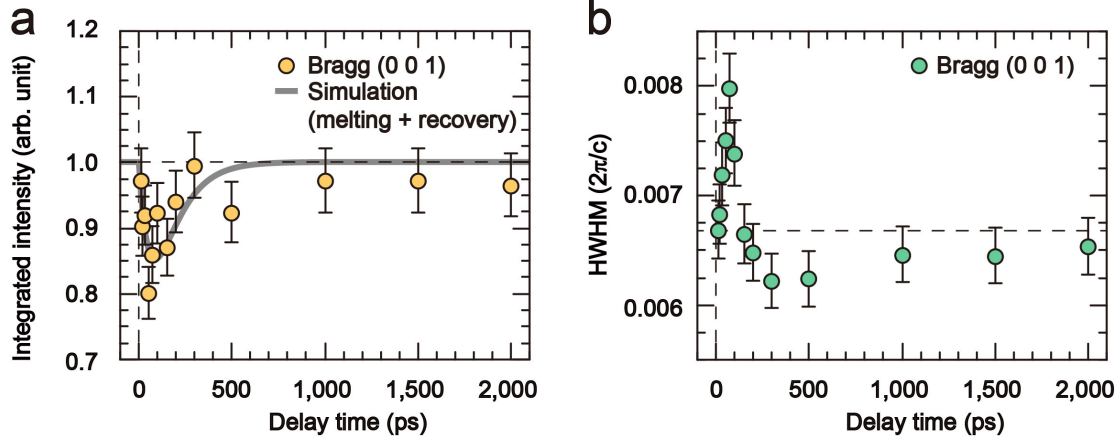


**Figure S2.** Temporal evolution of the (0 0 1) Bragg reflection. **a**, Reduction in the integrated intensity in the time scale of several tens of ps and recovery in several hundred ps to imply that thermalized lattice recovers before 1 ns. The simulated function (see the text) is drawn with the solid gray line. **b**, Half width at half-maximum of the (0 0 1) Bragg reflection shown in reciprocal lattice unit.

#### Supplementary Note 4. X-ray structure factor considering the $L_2^-$ coherent phonon at

$$\mathbf{Q} = \mathbf{Q}_{CDW}^{2 \times 2 \times 2}$$

X-ray scattering intensity for a given momentum transfer,  $\mathbf{Q}$ , is obtained using  $I(\mathbf{Q}) \sim |F(\mathbf{Q})|^2$ , with the  $F(\mathbf{Q})$  representing the structure factor. In general, the structure factor can be acquired by:

$$F(\mathbf{Q}) = \underbrace{\sum_n \exp[i\mathbf{Q} \cdot \mathbf{R}_n]}_{lattice} \underbrace{\sum_j f_j(\mathbf{Q}) \exp[i\mathbf{Q} \cdot \mathbf{r}_j]}_{unit\ cell} = \delta_{\mathbf{Q}=\mathbf{G}} \sum_j f_j(\mathbf{Q}) \exp[i\mathbf{Q} \cdot \mathbf{r}_j].$$

Here,  $\mathbf{R}_n$  and  $\mathbf{G}$  are real and reciprocal lattice vectors, respectively. The atomic form factor, spatial Fourier transformation of the charge distribution, is expressed as  $f_j$  and  $\mathbf{r}_j$  denotes the



$j$ -th atom in the unit cell. With this, any change in the X-ray structure factor caused by the  $L_2^-$  phonon can be obtained using,

$$\Delta F(\mathbf{Q}) \sim \delta_{\mathbf{Q}=\mathbf{G}} \sum_j f_{Cs}(\mathbf{Q}) \left\{ \underbrace{\exp(i\mathbf{Q} \cdot \mathbf{r}_j^{\text{PI}})}_{\text{Photoinduced}} - \underbrace{\exp(i\mathbf{Q} \cdot \mathbf{r}_j^{\text{int}})}_{\text{intact}} \right\}.$$

Here, the vibration of Cs atoms is considered to account for the  $L_2^-$  phonon exclusively. The position of Cs ions  $2 \times 2 \times 2$  unit cell is denoted using  $\mathbf{r}_j^{\text{PI}}$  and  $\mathbf{r}_j^{\text{int}}$  for the photoinduced displacements and intact positions, respectively.

We used the Taylor expansion to obtain the leading contribution as:  $\Delta F(\mathbf{Q}) \sim i\delta_{\mathbf{Q}=\mathbf{G}} f_{Cs}(\mathbf{Q}) \sum_j \mathbf{Q} \cdot (\mathbf{r}_j^{\text{PI}} - \mathbf{r}_j^{\text{int}})$ . As one notes, projected relative displacements of Cs ions along the X-ray scattering vector contribute to the intensity variation. This also confirms that symmetric two-up and two-down vibration of the Cs ions, corresponding to the native  $L_2^-$  phonon mode, cannot induce any intensity variation.

### Supplementary Note 5. Structure factor related to the diffuse peak near $\mathbf{Q} = \mathbf{Q}_{CDW}^{2 \times 2 \times 2}$

Given the number of unit cells  $N$ , the structure factor is defined as:

$$\sum_N \underbrace{\sum_j f_j(\mathbf{Q}) \exp[i\mathbf{Q} \cdot \mathbf{r}_{n,j}]}_{2 \times 2 \times 2 \text{ unit cell}} = \sum_N \exp[i\mathbf{Q} \cdot \mathbf{r}_n] \underbrace{\sum_j f_j(\mathbf{Q}) \exp[i\mathbf{Q} \cdot \mathbf{r}_{n,j}]}_{2 \times 2 \times 2 \text{ unit cell}}.$$

The displacement of unit cell,  $\mathbf{r}_n$  is expressed as:

$$\mathbf{r}_n = \mathbf{r}_n^0 + A_D \cos(\mathbf{Q}_D \cdot \mathbf{r}_n^0 - \varphi_S(t)).$$

Here,  $\mathbf{r}_n^0 = 2c_0 \mathbf{n}$  is position of  $2 \times 2 \times 2$  unit cell along the  $c$ -axis.  $A_D$ ,  $\mathbf{Q}_D$  and  $\varphi_S(t)$  are amplitude, wave vector and phase of short-range order respectively.

Using Jacobi–Anger expansion,  $\exp(ir \cos \theta) = \sum_n i^n J_n(r) \exp(in\theta)$  (with  $J_n(r)$  being the Bessel function of  $j$ -th kind) and considering up to first order for the same reason as long-ranged CDW. The measured intensity can be written as<sup>2,3</sup>:

$I(Q)$

$$= \left[ \sum_j f_j(Q) \exp[iQ \cdot r_n^0] \right]_{2 \times 2 \times 2 \text{ unit cell}}^2 \left[ |f(Q)|^2 - \underbrace{QA_D \sin(\alpha) |f(Q)f(Q + Q_D)|}_{\text{for } Q_D > 0} + \left( \frac{QA_D |f(Q + Q_D)|}{2} \right)^2 \right. \\ \left. + \underbrace{QA_D \sin(\alpha) |f(Q)f(Q - Q_D)|}_{\text{for } Q_D < 0} + \left( \frac{QA_D |f(Q - Q_D)|}{2} \right)^2 \right]$$

In the equation above, the term  $f(Q)$  and  $\alpha$  can be described as:

$$f(Q) = e^{i(N-1)Qr_n^0/2} \frac{\sin(NQr_n^0/2)}{\sin(Qr_n^0/2)}$$

and

$$\alpha = 2Qc_0[N - 1] - \varphi_S(t)$$

The asymmetry in diffuse peak at  $Q_D = \pm 0.005$  arises from the amplitude of defect and due to the phase of the short-ranged order in  $\sin(\alpha)$  term as described by the equation above.

### Supplementary Note 6. Cs ion's motion from time dependent DFT (TD-DFT) simulation

The temporal evolution of Cs ion's motion, calculated from TD-DFT simulation, is displayed in Fig. S3.

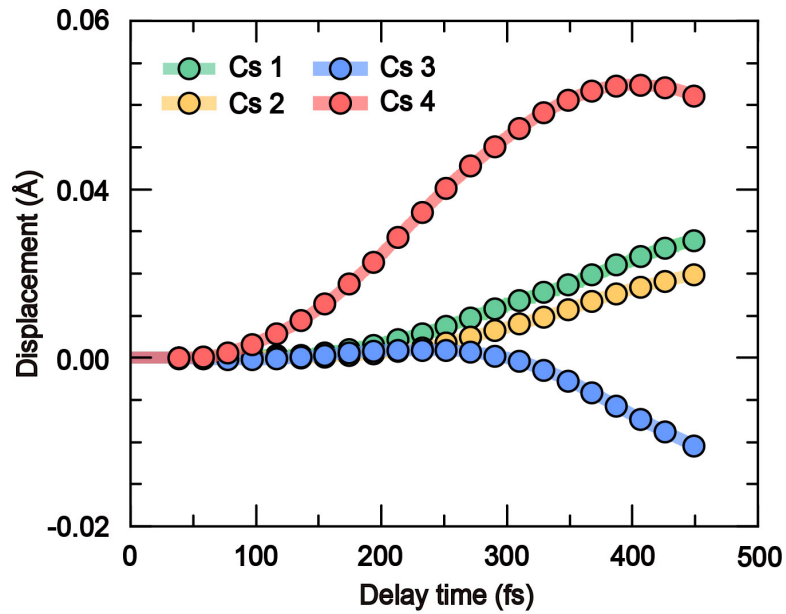


**Figure S3.** Cs ion's dynamics from TD-DFT. Each atom is labeled with Cs 1, Cs 2, Cs 3 and Cs 4, positioned at coordinates (0 0 0.5), (0.5 0 0.5), (0 0.5 0.5) and (0.5 0.5 0.5), respectively within the  $2 \times 2 \times 2$  unit cell in reciprocal lattice unit.

**Supplementary Note 7. Fluence dependence of coherent phonon frequency in  $2 \times 2 \times 2$  CDW ordering.**

The fluence dependence of modified  $L_2^-$  coherent phonon frequency is displayed in Fig. S4. Photoinduced softening in the phonon frequency is noted less than 2.5%.

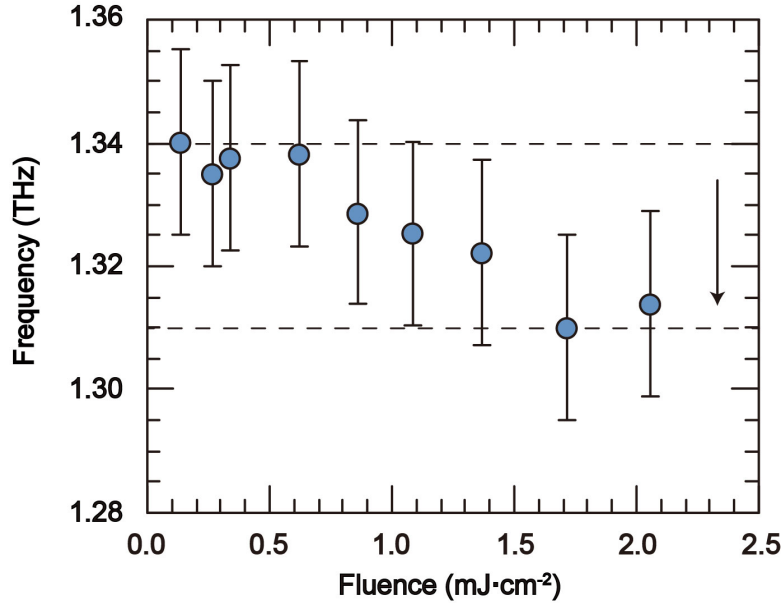


**Figure S4.** Fluence dependence of coherent phonon frequency. The frequency values are extracted from the simulated function for temporal evolution of  $2\times 2\times 2$  CDW intensity depicted in supplementary note 2. The upper and lower dot lines represent the maximum and minimum values from all data set. Very weak (2.5%) softening in the phonon frequency is noted.

### Supplementary Note 8. Selected $H$ and $L$ scans after the photoexcitation

The longitudinal scans along the  $(H\ 0\ 0)$  and  $(0\ 0\ L)$  direction are obtained around the  $(0.5\ 0\ 1)$  and  $(0.5\ 0\ 1.5)$  superstructure reflections representing the  $2\times 2\times 1$  and  $2\times 2\times 2$  CDW, respectively (Figs. S5 and S6). The  $H$  and  $L$  scan at  $Q = Q_{CDW}^{2\times 2\times 1}$  at 200 and 400 fs are similar in its shape to the intact CDW reflection except for decreased intensity. It indicates the intensity reduction results from reduced  $2\times 2\times 1$  CDW amplitude. In contrast, peak broadening appears significantly for the  $2\times 2\times 2$  CDW, and this diffuse peak can be attributed to Cs ions, consistent with the independence of the  $2\times 2\times 1$  CDW to Cs ion's displacement. In particular, the reflection at 400 fs consists of three peaks with the main peak at 1.5 having the width same as that of the intact structure, which immediately rules out the scenario of  $2\times 2\times 2$  CDW domain size increase by reducing the  $2\times 2\times 1$  CDW. Two side lobes developed symmetric to the center peak at 1.5 are from the phase slip in  $2\times 2\times 2$  CDW as described in the text.

In all scans, we did not observe any change in domain size with the photoexcitation along the  $ab$ -plane direction.

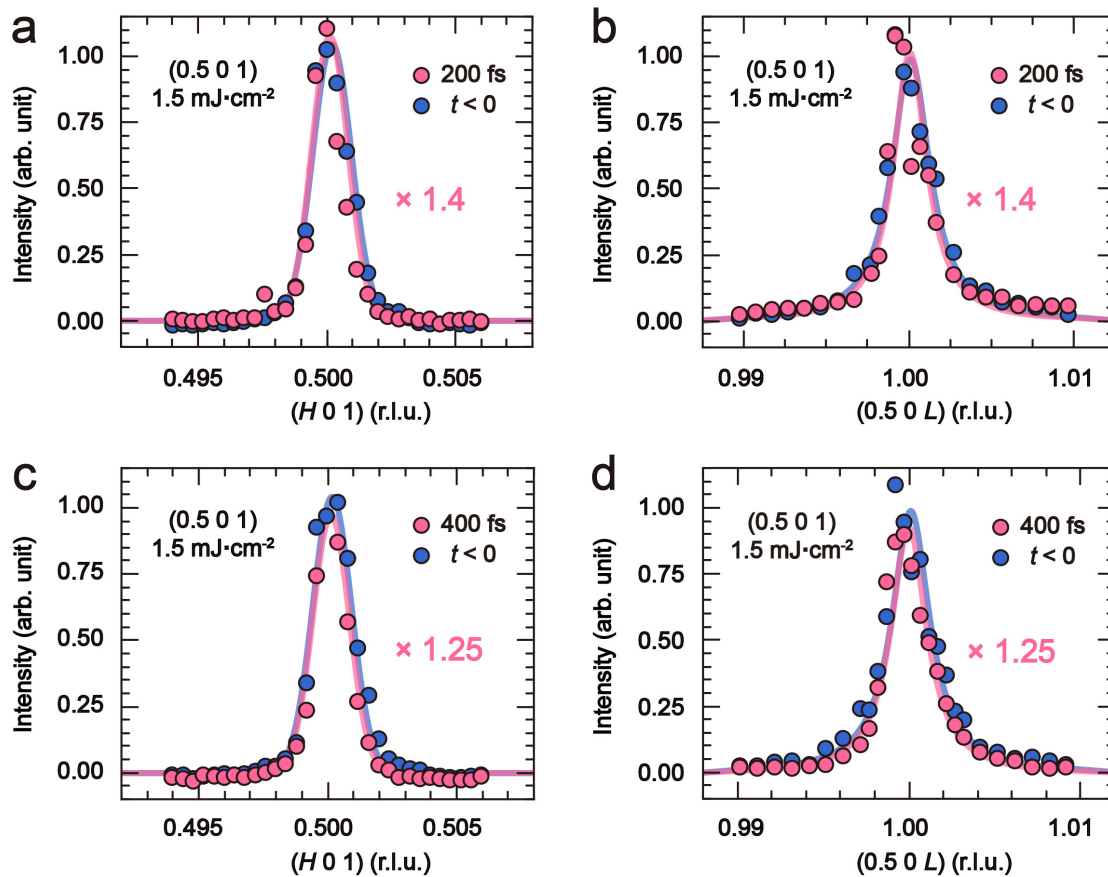


**Figure S5.**  $H$  and  $L$  directional scans along the  $2 \times 2 \times 1$  CDW reflection. Scans performed at 200 fs and 400 fs when the X-ray scattering intensity of the CDW reached minimum and quick recovery to have overdamping for  $2 \times 2 \times 2$  CDW, respectively.

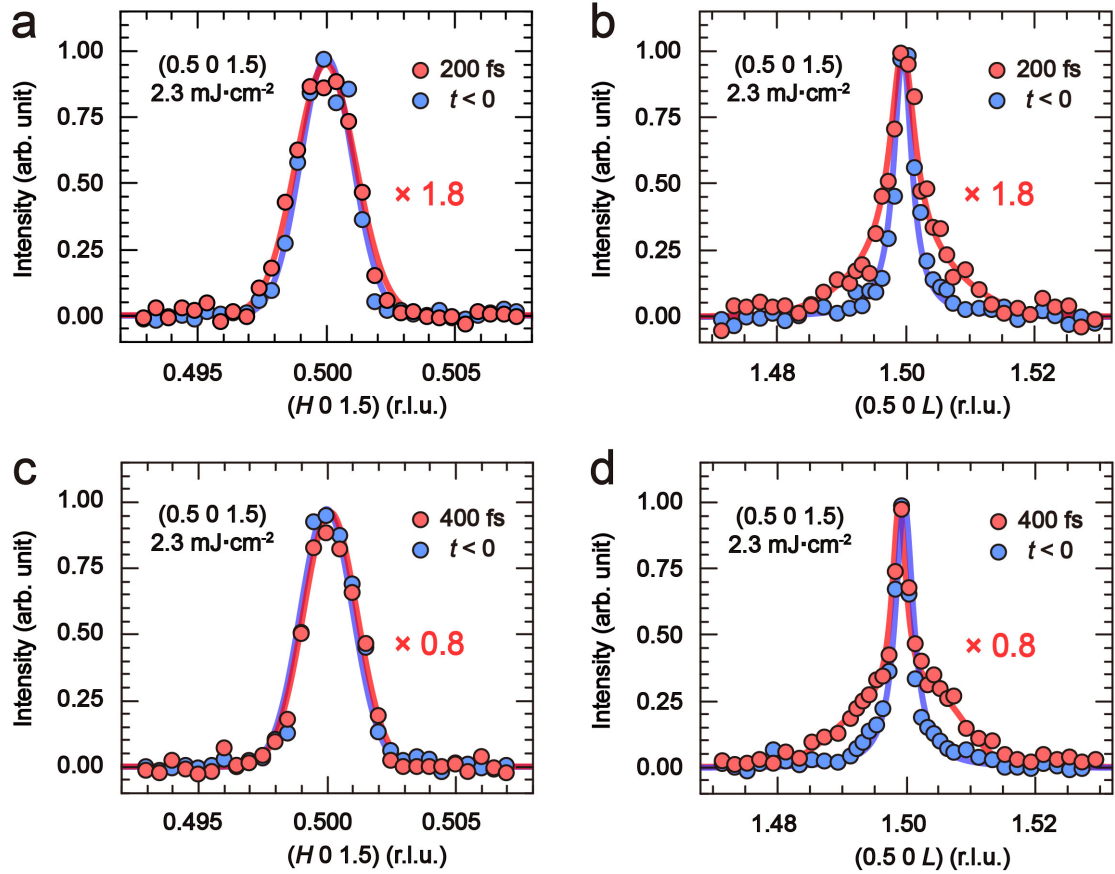


**Figure S6.**  $H$  and  $L$  directional scans along the  $2\times 2\times 2$  CDW reflection. Scans performed at 200 fs and 400 fs when the X-ray scattering intensity of the CDW reached minimum and quick recovery to have overdamping for  $2\times 2\times 2$  CDW, respectively. Upon photoinduced CDW melting, the X-ray scattering peak width increases in (b) informing the decreased domain size along the  $c$ -direction. A three-peak structure with two side lobes along the central peak is noted in (d) with the development of the phase slip.

### Supplementary Note 9. IR-laser fluence dependence of $L$ scan at 400 fs.

The laser fluence dependence of the X-ray reflection from the  $2\times 2\times 2$  CDW along the  $L$  direction are compared for the scan taken at 400 fs (Fig. S7). Increase in both of the main peak and the diffusive side lobes intensities are noted as the laser fluence increase, but the peak shape remains same.

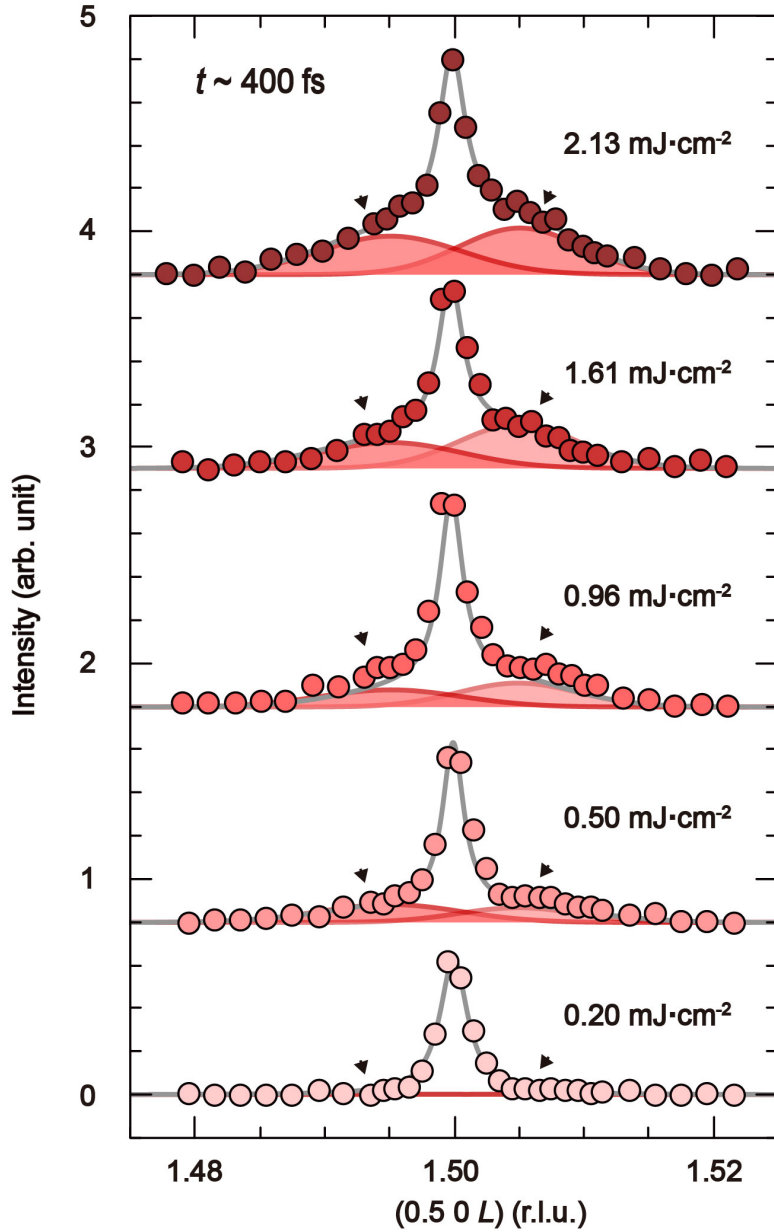


**Figure S7.** Fluence dependence of  $L$  scan along the  $(0.5\ 0\ 1.5)$  reflection from  $2\times 2\times 2$  CDW at 400 fs. Experimental data are fit to three Gaussians (grey) of one at the center representing the main CDW reflection and two diffuse reflections (red lines) symmetrically shifted from the center one. The diffusive side lobes are marked with arrow heads.

**Supplementary Note 10. X-ray structure factor of the  $2\times 2\times 2$  CDW at  $Q = Q_{CDW}^{2\times 2\times 1}$**

We calculate the X-ray structure factor considering the different configuration of the vanadium dimerization in the CDW phase. The calculation is performed using the vanadium ion's in-

plane displacements listed in the Table S1. Various CDW configurations are considered as shown in Fig. S8<sup>4,5</sup>.

<b>Atom</b>	<b><math>x/2a</math></b>	<b><math>y/2b</math></b>
$V_1$	$0.25 \pm \delta_1$	$0 \pm 2\delta_1$
$V_2$	$0 \pm 2\delta_1$	$0.25 \pm \delta_1$
$V_3$	$0.25 \mp \delta_2$	$0.25 \mp \delta_2$
$V_4$	0.5	$0.25 \mp \delta_2$
$V_5$	$0.25 \mp \delta_2$	0.5
$V_6$	$0.75 \mp \delta_1$	$0 \mp 2\delta_1$
$V_7$	$0.75 \mp \delta_1$	$0.25 \pm \delta_1$
$V_8$	$0.75 \pm \delta_2$	0.5
$V_9$	$0 \mp 2\delta_1$	$0.75 \mp \delta_1$
$V_{10}$	$0.25 \pm \delta_1$	$0.75 \mp \delta_1$
$V_{11}$	0.5	$0.75 \pm \delta_2$
$V_{12}$	$0.75 \pm \delta_2$	$0.75 \pm \delta_2$

**TABLE S1.** Atomic positions of vanadium in  $2 \times 2$  SOD and TrH dimerization



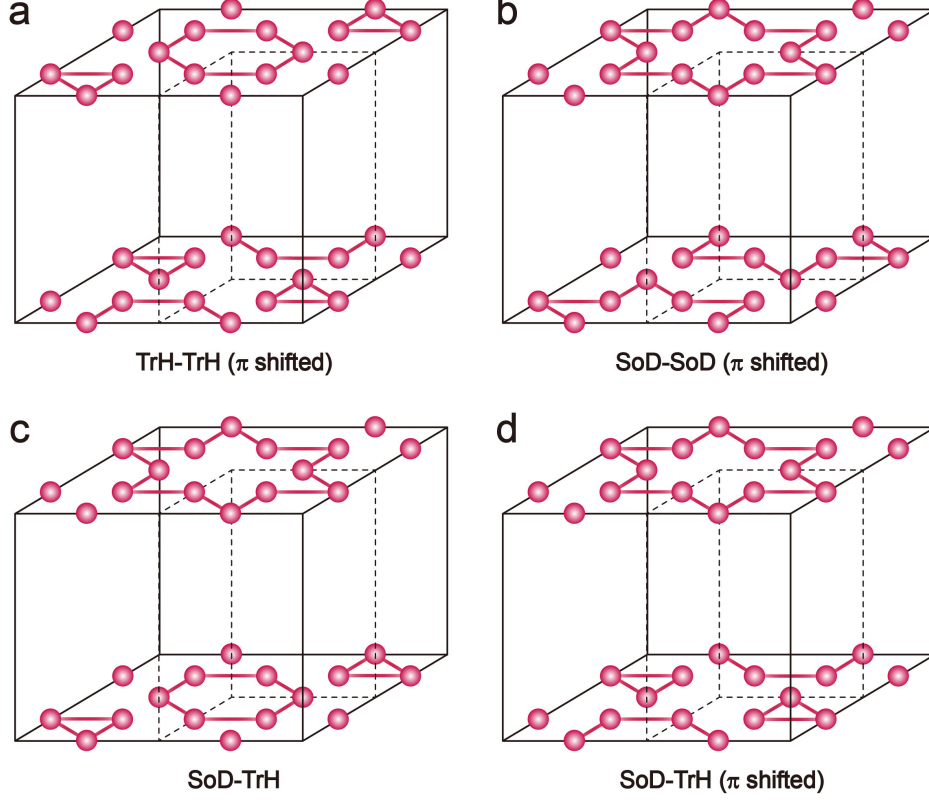


**Figure S8. a-d**, All possible CDW configurations making the  $2 \times 2 \times 2$  superstructure are shown. **a**, TrH-TrH ( $\pi$ -shifted) **b**, SoD-SoD ( $\pi$ -shifted) **c**, SoD-TrH (3), **d**, SoD-TrH ( $\pi$ -shifted).

The X-ray structure factor for each CDW configuration can then be obtained as:

$$F(Q) = \delta_{Q=G} \sum_j f_V(Q) \left[ \underbrace{\exp[iQ \cdot r_j^{TrH}]}_{TrH} + \underbrace{\exp[iQ \cdot (r_j^{TrH} + [a_0 \ 0 \ c_0])]}_{\pi\text{-shifted } TrH} \right]$$

$$F(Q) = \delta_{Q=G} \sum_j f_V(Q) \left[ \underbrace{\exp[iQ \cdot r_j^{SoD}]}_{SoD} + \underbrace{\exp[iQ \cdot (r_j^{SoD} + [a_0 \ 0 \ c_0])]}_{\pi\text{-shifted } SoD} \right]$$

$$F(Q) = \delta_{Q=G} \sum_j f_V(Q) \left[ \underbrace{\exp[iQ \cdot r_j^{SoD}]}_{SoD} + \underbrace{\exp[iQ \cdot (r_j^{TrH} + [0 \ 0 \ c_0])]}_{TrH} \right]$$

$$F(Q) = \delta_{Q=G} \sum_j f_V(Q) \left[ \underbrace{\exp[iQ \cdot r_j^{SoD}]}_{SoD} + \underbrace{\exp[iQ \cdot (r_j^{TrH} + [a_0 \ 0 \ c_0])]}_{\pi\text{-shifted } TrH} \right].$$

Considering only first order phase term,  $e^x \simeq 1 + x$  under condition of  $\mathbf{Q} \cdot \boldsymbol{\delta}_{1,2} \ll 1$ , the structure factor  $F(Q)$  at  $Q = (l \pm 0.5 \ 0 \ n)$  corresponding to the  $Q = Q_{CDW}^{2 \times 2 \times 1}$  is zero ( $l$  and  $n$

is integer). It confirms that the possibility of observing a  $2\times 2\times 2$  superstructure domain at  $Q = Q_{CDW}^{2\times 2\times 1}$  can be excluded.

### References:

1. Allen, P. B. Theory of thermal relaxation of electrons in metals. *Phys. Rev. Lett.* **59**, 1460–1463 (1987).
2. Singer, A. *et al.* Photoinduced Enhancement of the Charge Density Wave Amplitude. *Phys. Rev. Lett.* **117**, 056401 (2016).
3. Singer, A. *et al.* Condensation of collective charge ordering in chromium. *Phys. Rev. B* **91**, 115134 (2015).
4. Christensen, M. H., Birol, T., Andersen, B. M. & Fernandes, R. M. Theory of the charge density wave in  $AV_3Sb_5$  kagome metals. *Phys. Rev. B* **104**, 214513 (2021).
5. Kang, M. *et al.* Charge order landscape and competition with superconductivity in kagome metals. *Nat. Mater.* **22**, 186–193 (2023).